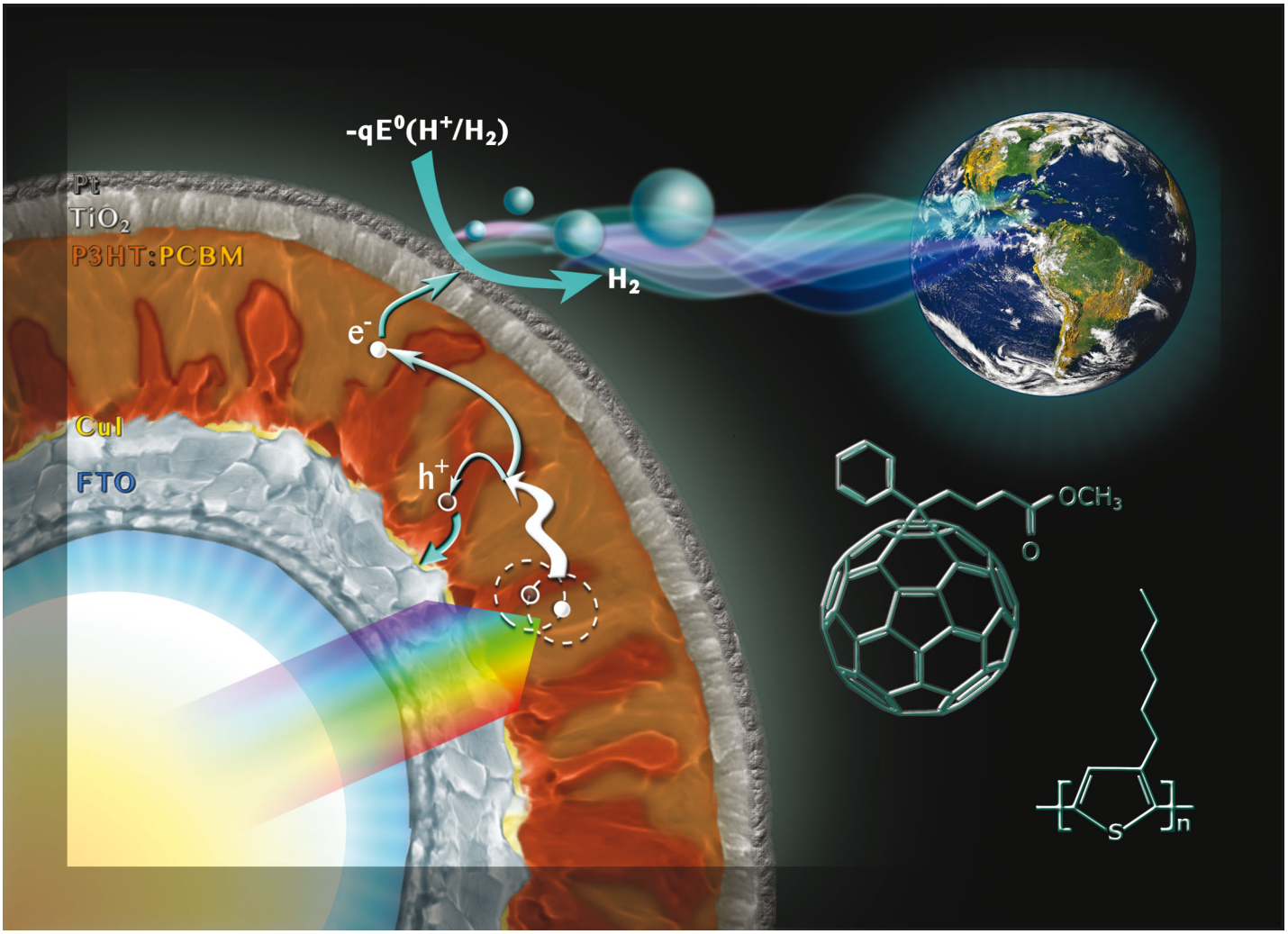

Showcasing research from the laboratories of Dr Maria Rosa Antognazza and Dr Fabio Di Fonzo at Center for Nano Science and Technology, Italian Institute of Technology.

Polymer-based photocathodes with a solution-processable cuprous iodide anode layer and a polyethyleneimine protective coating

Photoelectrochemical production of solar fuels is currently challenging and no technologically viable solutions have been found so far. We demonstrate that conjugated polymers, in synergy with inorganic charge selective layers, sustain efficient and reliable hydrogen production upon solar light excitation, making them an interesting alternative to fully inorganic systems.

Support acknowledged from EU under through the FET programme, collaborative project PHOCS, grant agreement no. 309223.

Image designed by Isabella McKenna, Center for Nano Science and Technology, Italian Institute of Technology.

As featured in:

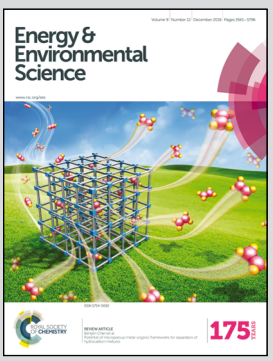

See Fabio Di Fonzo, Maria Rosa Antognazza *et al.*, *Energy Environ. Sci.*, 2016, **9**, 3710.

ROYAL SOCIETY OF CHEMISTRY

www.rsc.org/ees

Registered charity number: 207890

Energy & Environmental Science

PAPER

View Article Online
View Journal | View Issue

Cite this: *Energy Environ. Sci.*, 2016, **9**, 3710

Polymer-based photocathodes with a solution-processable cuprous iodide anode layer and a polyethyleneimine protective coating†

Hansel Comas Rojas,[ad] Sebastiano Bellani,[ab] Francesco Fumagalli,[a] Gabriele Tullii,[a] Silvia Leonardi,[a] Matthew T. Mayer,[c] Marcel Schreier,[c] Michael Grätzel,[c] Guglielmo Lanzani,[ab] Fabio Di Fonzo*[a] and Maria Rosa Antognazza*[a]

Received 9th June 2016,
Accepted 28th July 2016

DOI: 10.1039/c6ee01655c

www.rsc.org/ees

Organic semiconductors have been proven to be suitable for efficient photovoltaic generation during the last decade but have been scarcely assessed as photoelectrochemical devices. In this work we present the fabrication and characterization of a new efficient hybrid organic/inorganic photocathode for hydrogen evolution showing both a positive onset potential (+0.702 V *vs.* RHE) and a maximum power point (+0.303 V *vs.* RHE). We demonstrate that a conventional P3HT:PCBM bulk heterojunction architecture enclosed between a solution-processed cuprous iodide hole selective layer and a Pt-decorated nanostructured TiO_2 layer can efficiently photogenerate hydrogen under acidic conditions under simulated 1 Sun illumination. This architecture showed initial photocurrents as high as 8 mA cm^{-2} at 0 V *vs.* RHE, IPCE above 50%, 100% faradaic efficiency and an ideal ratiometric power-saved figure of merit equal to 1.21%. Finally, with the addition of a solution-processed polyethyleneimine protective coating, we improved the device stability. This work paves the way to the use of hybrid organic/inorganic photocathodes for efficient solar hydrogen generation.

Broader context

The photoelectrochemical route is the most direct one towards solar energy conversion and hence the production of hydrogen as an energy carrier. The archetypal photoelectrochemical device must produce under solar illumination around 1.6 V to drive the unassisted water splitting reaction and steadily generate a photocurrent of several mA cm^{-2} in an aqueous environment. Pursuing an efficient photocathode is of key importance and several candidates have been successfully realized but relying on very sophisticated systems and precious materials. On the other hand, the use of conjugated semiconducting polymers is a viable alternative, which gains more attention every year. We have pursued the fabrication of a hybrid organic/inorganic photocathode by using an archetypal organic bulk heterojunction sandwiched between inorganic charge selective layers. What makes this approach unique is the use of a water insoluble cuprous iodide hole selective layer and the implementation of a hyperbranched polyethyleneimine overcoating to limit catalyst detachment, both depositions being fast and low temperature solution-processable. Competitive figures of merit were thus obtained. Our approach broadens the most traditional use of semiconducting polymers as photovoltaic materials and proposes them as a feasible, scalable and cost competitive alternative towards solar hydrogen generation.

Introduction

One of the main challenges facing humankind in this century is to supply the world's population with sufficient energy to fulfill the desired living standards.[1] Solar photoelectrochemical (PEC) hydrogen production could in principle provide a clean, cost-effective and domestically produced energy carrier, but still faces technical challenges.[2,3] In order for hydrogen production to occur efficiently and sustainably, several stringent criteria must be met simultaneously both by the semiconductor and by the PEC device as a whole. The semiconductor system must generate sufficient voltage upon irradiation to split water, have strong optical absorption in the IR-visible range, with band edge potentials at the surfaces which straddle the hydrogen and oxygen redox potentials, and enable efficient charge transfer from the surface of the semiconductor to the redox species in solution. In addition, the system must exhibit long-term stability against corrosion in aqueous electrolytes,[2–4] and use

[a] *Center for Nano Science and Technology @PoliMi, Istituto Italiano di Tecnologia, Via Pascoli 70/3, 20133 Milano, Italy. E-mail: fabio.difonzo@iit.it, mariarosa.antognazza@iit.it*
[b] *Politecnico di Milano, Dip.to di Fisica, P.zza L. da Vinci 32, 20133 Milano, Italy*
[c] *Laboratory of Photonics and Interfaces, Institute of Chemical Sciences and Engineering, Ecole Polytechnique Fédérale de Lausanne, CH-1015 Lausanne, Switzerland*
[d] *Higher Institute for Applied Sciences and Technologies (INSTEC), Salvador Allende y Luaces, 6163, La Habana, Cuba*

† Electronic supplementary information (ESI) available: Fig. S1–S10. See DOI: 10.1039/c6ee01655c

non-precious and non-toxic materials.[5] To date, no materials system satisfies all of these technical requirements, whereas some elaborate systems, *e.g.* tandem structures or coupled photovoltaic–electrolysis systems, have surpassed the 10% solar-to-hydrogen (STH) energy conversion efficiency target, the benchmark for PEC hydrogen production.[6–9]

Among the different PEC configurations that can be adopted,[10] the realization of an efficient and durable photocathode able to generate hydrogen from solar-driven water splitting would be highly desirable. This, however poses technical hurdles, especially regarding the material choice. A variety of p-type materials have been pursued, spanning from silicon[11] to phosphides[6,12] and chalcogenides,[13] while copper oxide (Cu_2O) has arisen as a competitive earth-abundant semiconductor.[14,15] However, desirable features for photocathodes still remain elusive. Focusing on radically different approaches and investigating unprecedented light-harvesting materials is thus urgently required.

Organic semiconductors provide a valuable opportunity for solar fuel generation *via* the PEC route. They are optimal light absorbers and support charge generation, as successfully demonstrated in photovoltaic (PV) conversion, with power conversion efficiencies over 10%.[16,17] Their electronic energy levels can be finely tuned, in order to closely match the redox potentials required for water splitting reactions.[18] They are solution-processable materials compatible with roll-to-roll deposition techniques, thus allowing the scaling-up of devices over size and number.[19]

One main issue concerning the application of organic semiconductors is their stability in air or in liquid, with the main degradation phenomena attributed to the oxidation of the semiconductor/metallic electrode interface.[20] In general, protection of the semiconductor material and careful engineering of the interfacial layers facing the electrolyte have been recognized as critical steps towards stability and performance[21] in each kind of approach.[9,22,23] However, recent evidence demonstrated that a prototypical conjugated polymer, namely regio-regular poly(3-hexylthiophene-2,5-diyl) (rr-P3HT), fully preserves its optoelectronic capabilities in an aqueous environment, particularly with reference to the charge generation process.[24] rr-P3HT has a direct band gap of 1.9 eV, close to the optimum for a tandem PEC device,[5,25] and a LUMO (Lowest Unoccupied Molecular Orbital) level several hundreds of mV above the hydrogen redox potential. These properties make rr-P3HT an optimal candidate for the realization of a polymer-based photocathode.[26] Accordingly, preliminary results have been reported by a few groups, adopting rr-P3HT blended with the fullerene derivative [6,6]-phenyl C61 butyric acid methyl ester (PCBM) in a bulk heterojunction architecture (BHJ).[27–31] In these reports, the importance to find suitable interfacial layers, and in particular better performing hole selective materials was often recognized, especially for poly(3,4-ethylenedioxythiophene) doped with polystyrene sulfonate (PEDOT:PSS)[32] and more recently for molybdenum oxide (MoO_3).[33]

The use of a more stable material while keeping the preparation of the device based on solution-processed techniques and low temperature processing protocols is highly desirable. Novel yet simple protective strategies, capable of increasing the temporal durability of the photocathode, would be equally appealing.

Here, we face the problem of an efficient hole selective layer with higher performance and stability, without compromising deposition processing easiness and potential scalability over large areas. We report on the fabrication and characterization of a hybrid organic/inorganic hydrogen evolving photocathode based on the conventional P3HT:PCBM bulk heterojunction architecture, but using a cuprous iodide (CuI) solution-based layer as the hole selective contact.[34] p-Type γ-phase CuI, as recently reviewed,[35] is a material that meets all the requirements mentioned above in terms of cost, processability and environmental stability. The electron-selective and transport layer is a nanostructured amorphous titanium dioxide (TiO_2) deposited by Pulsed Laser Deposition (PLD),[36,37] and decorated by a thin, magnetron sputtered, platinum (Pt) electrocatalyst layer. Photoelectrochemical, optical and structural characterization was used to investigate both the device operation and to gain an insight into the photophysical processes occurring in our systems. Spectroscopic measurements carried out on polymer-based photocathodes further corroborated the assessment of CuI as an optimal candidate for highly efficient hole collection. A solution processed, protective coating based on branched polymer polyethyleneimine (PEI) was also adopted to improve the device stability.

Our results lead to a competitive proof-of-concept hybrid organic/inorganic hydrogen evolving photocathode, as a promising step towards an efficient, all-solution processed and fully scalable device.

Experimental

Device fabrication

Devices were fabricated on commercial fluorine-doped tin oxide (FTO) coated soda-lime glass substrates (purchased from Dyesol Italia SRL, dimensions 20 × 12 × 2.1 mm, FTO thickness 250 nm and sheet resistance 15 Ohm sq^{-1}). Substrates were cleaned by subsequent ultrasonic baths lasting 20 minutes each (alkaline detergent HELLMANEX 3%, ultrapure water, acetone, isopropyl alcohol). After each step the substrates were dried under a nitrogen flow. A subsequent overnight drying at 130 °C allowed full solvent evaporation. An oxygen plasma treatment (DIENER, 40 Pa, 100 W for 20 minutes) completed the substrate preparation procedure.

Hybrid organic/inorganic photocathodes were realized by subsequent deposition of different layers, according to the following architecture: FTO/CuI/P3HT:PCBM/TiO_2/Pt. Complementary devices without hole or electron selective or catalyst layers were also fabricated as a reference. Cuprous iodide (CuI, Sigma Aldrich, 97% purity) was dissolved in acetonitrile (Sigma Aldrich, ACS grade) at 10 g L^{-1} concentration. The solution was filtered by using PTFE filters with a cut-off dimension of 450 nm (PALL technologies). CuI deposition was carried out by spin coating in one single step (3000 rpm rotation speed for 60 s). The active layer is constituted by conjugated polymer regio-regular poly(3-hexylthiophene-2,5-diyl)

(rr-P3HT, purchased from Sigma Aldrich and used without further purification, molecular weight M_w 15 000–45 000, purity 99.995%) acting as the electron donor, and the fullerene derivative [6,6]-phenyl C61 butyric acid methyl ester (PCBM, purchased from Nano-C Inc.), acting as the electron acceptor. Both were individually dissolved in chlorobenzene (Sigma Aldrich, ACS grade) and then mixed at 1 : 1 wt ratio and 25 mg mL^{-1} on a polymer basis. The blend solution was stirred overnight at 50 °C. The active layer was spin-coated on top of the CuI layer in a two-step process (800 rpm for 3 s, followed by 1600 rpm for 60 s). The active layer thickness is 220 ± 10 nm (as measured by means of an Alpha-Step IQ surface profilometer), appropriate for optimal light absorption under simulated 1 Sun illumination. The electron selective layer (amorphous TiO_2) was deposited by pulsed laser deposition starting from a titania target (Testbourne, 99.99% purity) in an Ar/H_2 atmosphere (3.1% mol H_2 content) at a pressure of 15 Pa. The vacuum chamber was evacuated to a base pressure of $\sim 3 \times 10^{-3}$ Pa before deposition. A pulsed excimer laser (Coherent KrF, λ = 248 nm) was operated at a pulse repetition rate of 20 Hz with 400 mJ per pulse and a fluence of 2.5 J cm^{-2}. A pulsed-DC magnetron sputtering cathode with adjustable repetition frequency and duty cycle was used for platinum deposition (Testbourne, 99.99% purity). The vacuum chamber was evacuated to a base pressure of $\sim 3 \times 10^{-3}$ Pa before each deposition. For Pt deposition discharge the operating pressure was 15 Pa and Ar gas flow was 410 sccm. The target–substrate distance was fixed at 80 mm. A fixed shadow mask defines the catalyst area being equal to 0.72 cm^2. Finally, for the realization of a solution-processable protective layer, we employed branched polyethyleneimine (PEI, M_w 25 000 g mol^{-1}, Sigma Aldrich), dissolved in ethanol at 0.1% concentration and spin coated on top of full devices at a speed of 2000 rpm for 60 s. Post thermal annealing at 130 °C per 10 minutes in an inert atmosphere completed the fabrication of the hybrid photocathode.

Device characterization

The thickness of the layers was also confirmed by cross-sectional Scanning Electron Microscopy (SEM) measurements using a Zeiss SUPRA40 field-emission SEM instrument under an operating voltage of 5 kV and a working distance of 2 mm. Height and phase maps of FTO and FTO/CuI layers were evaluated by Atomic Force Microscopy (AFM) using an Agilent 5500 Atomic Force Microscope in tapping mode. Scans were performed over a length scale of 1 × 1 μm^2 at a scan speed of 0.2 lines per s. Root Mean Square (RMS) roughness values were calculated from AFM topography images using Gwyddion 2.35 software.

Work function data were obtained by using a commercial kelvin probe system (KPSP020, KP Technologies Inc.). Samples were measured in air and at room temperature and both a clean gold surface (WF = 4.8 eV) and a graphite sample (HOPG, highly ordered pyrolytic graphite, WF = 4.6 eV) were used as independent references for the probe potential. UV-visible transmittance and absorption spectra of the materials used in the photocathodes were recorded by using a Perkin-Elmer Lambda 1050 spectrophotometer.

Spectroscopic measurements

Intensity Modulated Photocurrent/Photovoltage Spectroscopies (IMPS/IMVS) were performed by coupling the photoelectrochemical station (see below for the details) to a FRA32M module (Metrohm) connected to an Autolab LED driver kit which powered a 530 nm high-power LED. The light intensity was modulated by 10% of the DC light intensity, fixed at 29.54 mW cm^{-2}, as measured using a calibrated Si-photodiode (FDS100, THORLABS). The IMPS measurements were performed at 0 V *vs.* RHE in the frequency range of 1 Hz to 10^5 Hz while the IMVS spectra were acquired under open circuit conditions in the frequency range of 1 Hz to 10^4 Hz. The data were plotted in accordance with the standard electrochemical notation, which means that cathodic and anodic currents are defined as negative and positive, respectively, while positive and negative photopotentials mean accumulation of holes and electrons, respectively, at the back contact. The Kronig–Kramers (KK) test was used to evaluate the time stability and the linearity of the system.[38] The experimental data points were fitted using a special complex model (KK function) which always satisfies the KK relations. This implies that if the measured data set can be represented with this model, then the data set should also satisfy the KK assumptions. The result of the test is the value of pseudo χ_{ps}^2, the sum of the squares of the relative residuals. In the frequency ranges adopted here, we obtained χ_{ps}^2 values approaching 10^{-5}, which indicates an excellent fit. All the data were analyzed using the NOVA 1.11 and OriginPro 8.0 software.

Photoelectrochemical measurements

Photoelectrochemical measurements were carried out at room temperature in a flat-bottom fused silica cell in a three-electrode configuration using an Autolab PGSTAT302N potentiostat/galvanostat station, equipped with the Nova 1.8 (Metrohm) software package. A Pt wire was used as the counter-electrode and Ag/AgCl, sat. KCl was used as the reference electrode. Measurements were performed in 50 mL aqueous solution of 0.1 M H_2SO_4 (Sigma-Aldrich, 99.999% purity): 0.1 M Na_2SO_4 (Sigma-Aldrich, purity 99.0%), at pH 1.0. Oxygen was purged from the electrolyte solutions by flowing nitrogen gas throughout the liquid volume using a porous frit at least 30 minutes before starting measurements. A constant, slight nitrogen flow was maintained afterwards for the whole duration of experiments, to avoid re-dissolution of molecular oxygen in the electrolyte. Potential differences between the working electrode and the reference electrode are reported with respect to the RHE scale using the Nernst equation. A 300 W xenon light source (Lot Quantum Design, model LS0306), equipped with AM 1.5 G filters, was used to simulate solar illumination conditions at the glass substrate side of the samples inside the test cell.

Linear Sweep Voltammetry (LSV) has been employed to evaluate the response of devices in the dark and under chopped illumination. Voltage was swept starting above the open circuit potential of the electrochemical cell (OCP) towards cathodic potentials below 0 V *vs.* RHE at a scan rate of 10 mV s^{-1}. Stability tests have been performed by running potentiostatic

chrono-amperometries (CA) at 0 V *vs.* RHE, under continuous illumination, and monitoring dark current values from time to time.

Incident photon-to-electron conversion efficiency (IPCE) measurements were performed using a light source 300 W xenon lamp (Cermax PE 300 BUV) and a monochromator (Bausch & Lomb, FWHM 10 nm) between 350 nm and 700 nm. The photocathode was fixed inside a test cell equipped with a quartz window and illuminated from the glass substrate side by using a shadow mask with 0.64 cm^2 aperture. The photocurrent response data were collected by running CA measurements in three-electrode configuration at 0 V *vs.* RHE and at pH 1, being further normalized against a calibrated silicon photodiode (THORLABS, FDS-100) to determine the IPCE values at each wavelength.

For analysis of the evolved gas products, the hybrid photocathode was fixed inside a gas-tight test cell with a quartz window and illuminated from the glass substrate side by a

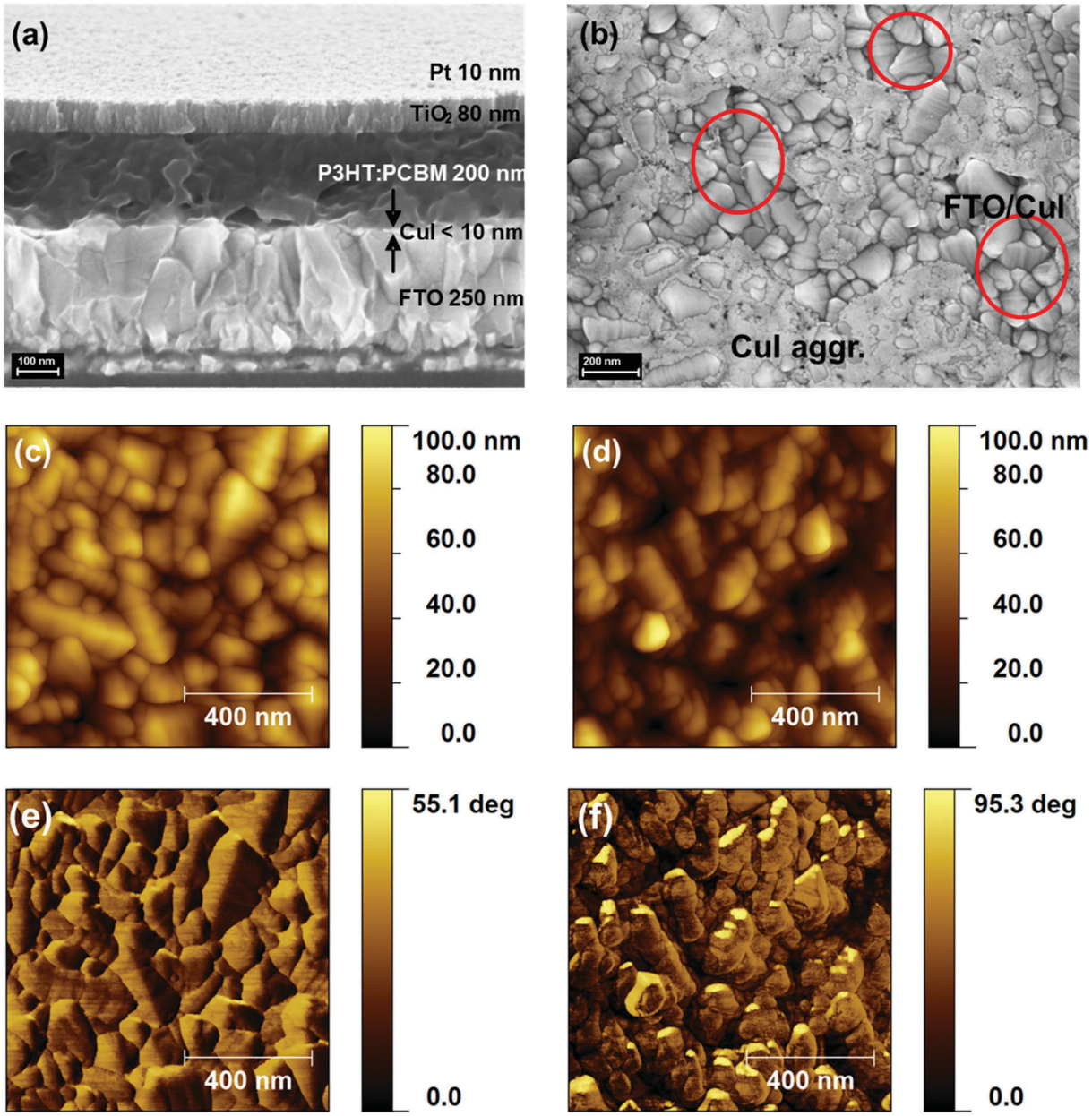

Fig. 1 Hybrid photocathode FTO/CuI/P3HT:PCBM/TiO_2/Pt microstructure. (a) Cross-sectional SEM view of the hybrid organic/inorganic photocathode showing its inner structure and nominal thicknesses of each layer (scale bar 100 nm). (b) Top SEM view of a CuI layer deposited on top of the FTO substrate (scale bar 200 nm). Two different morphologies are evidenced, one characterized by the presence of a very thin CuI layer and the other one by the formation of CuI aggregates. (c–f) Atomic Force Microscopy topography (c and d) and phase images (e and f) of bare FTO (c and e, respectively) and FTO/CuI (d and f, respectively). Images of FTO/CuI were acquired in correspondence to regions that more closely resemble the typical FTO morphology like the ones evidenced by the red circles in panel (b). Scale bar: 400 nm.

450 W xenon lamp (Osram, ozone-free), equipped with a KG3 filter (Lot QD) and calibrated to 1 sun illumination intensity by a Si photodiode as well. Measurements were conducted by running CA measurements in three-electrode configuration at 0 V *vs.* RHE while maintaining rapid magnetic stirring. Helium gas at 20 mL min^{-1} flow was continuously bubbled through the cell with the out-flow periodically injected into a gas chromatograph (GC, TRACE Ultra with a PDD detector, Thermo Scientific; ShinCarbon ST column, Restek) for in-line characterization of evolved hydrogen. The Pt wire counter electrode was held behind a porous ceramic frit to minimize product crossover. The GC response was calibrated within the same cell and gas flow conditions using a dedicated Pt wire under galvanostatic hydrogen evolution at known rates.

Results and discussion

Architecture of the hybrid organic/inorganic photocathode

The full structure of the hybrid organic/inorganic photocathode comprises a transparent conductive substrate (FTO-coated glass), a hole selective layer based on CuI, the photo-active, charge generating layer, based on the polymer blend P3HT:PCBM, an electron-selective layer (TiO_2) and a very thin catalyst layer (Pt). The cross-sectional SEM image (Fig. 1a) shows very well-defined interfaces, with the exception of the CuI layer, whose small thickness (<10 nm, see Fig. S1, ESI†) makes the corresponding interfaces difficult to appreciate at device-scale magnification. A top view SEM image (Fig. 1b) and Atomic Force Microscopy images (Fig. 1d) of FTO/CuI films provide a more detailed characterization of the CuI film surface topography and roughness as compared to FTO surfaces (Fig. S2, ESI† and Fig. 1b showing SEM top views and Fig. 1c and d, showing AFM topography images for FTO and FTO/CuI, respectively). The coverage of FTO substrates by CuI thin layers can be appreciated by means of AFM phase imaging, exhibiting a significant phase shift in the case of FTO/CuI samples (Fig. 1f), with respect to bare FTO substrates (Fig. 1e). Similar evidence was provided by Shao *et al.* when evaluating different layer thicknesses during vacuum evaporation of CuI.[39] From the SEM images the presence of CuI aggregates is also evident, whose extent could not be reduced either by filtering the solution or modifying the spin-coating protocol. However, more homogeneous films might actually be obtained by decreasing the solution concentration, but at the expense of the overall performances of the device, as recently demonstrated in the case of solar cells based on P3HT:PCBM and employing different CuI layer thicknesses.[40]

The hybrid organic/inorganic architecture was specifically designed to have a favourable energetic alignment, matching the electrochemical potential needed for efficient HER, and to provide a built-in potential gradient able to separate electrons and holes while avoiding recombination losses (Fig. 2a). In particular, the work function of CuI, as measured by Kelvin Probe studies (4.89 ± 0.04 eV) and in line with recent literature,[40] is expected to provide for efficient hole collection when in contact with P3HT. Actually, values between 5.1 and 5.4 eV have been reported for thicker films.[34,39]

The transmittance spectra of the FTO substrate and the FTO/CuI layer are shown in Fig. 2b. The CuI layer contributes an almost negligible decrease in transmittance as compared to the bare FTO substrate over the whole visible range, with transmittance values approaching 80%, nearly ideal for efficient light absorption by the photo-active layer when illuminated through the substrate. In the transmittance spectrum of the full device, the characteristic absorption features of rr-P3HT (maximum absorption peak at 500 nm, vibrational replicas at 550 nm and 600 nm) are clearly visible. The low transmittance is due to light absorption by the metallic Pt layer, since the nanostructured TiO_2 layer exhibits high transmittance in the visible spectral range (see Fig. S3, ESI†). The absorption spectrum of the P3HT:PCBM film is also shown

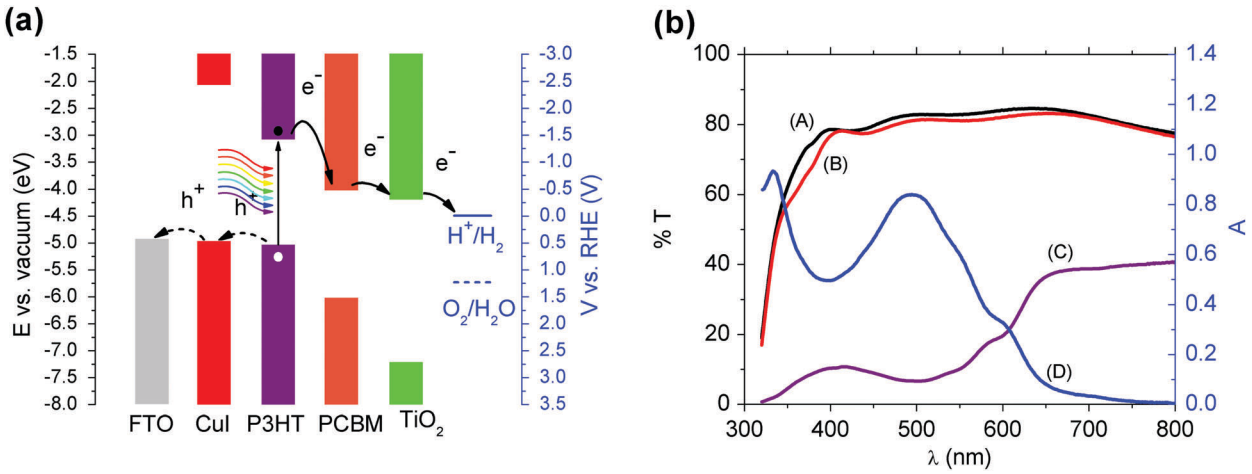

Fig. 2 (a) Energy band edge positions of materials assembled in the hybrid photocathode. The P3HT:PCBM layer, in the bulk heterojunction configuration, efficiently absorbs light and generates charges. CuI and TiO_2 act as hole and electron selective layers, respectively. Redox levels for both the hydrogen evolution reaction (HER, solid line) and the oxygen evolution reaction (OER, dashed line) are also shown. (b) Transmittance spectra of: (A) bare FTO, (B) FTO/CuI and (C) full device. Absorbance of the neat P3HT:PCBM active layer (trace D, right *Y*-axis).

as a control reference. The electrochemical stability of FTO/CuI and FTO/CuI/P3HT:PCBM samples was assessed by cyclic voltammetry experiments (Fig. S4, ESI†).

Spectroscopic characterization of the device

The realization of an efficient photocathode relies on the accumulation and extraction of energetic electrons (holes) at the interface with the electrolyte and holes at the back contact. The interfacial recombination rates and charge transfer kinetics are thus the most important factors to be considered, and they are mainly determined by the selection of charge-selective layers. We directly measured kinetic parameters in the hybrid photocathodes by making use of Intensity Modulated Photocurrent Spectroscopy (IMPS) and Intensity Modulated Photovoltage Spectroscopy (IMVS). Both IMPS and IMVS are forms of impedance spectroscopy, which measure the periodic modulation of the photocurrent and photovoltage, respectively, in response to a small sinusoidal perturbation of the light intensity superimposed on DC illumination.[41] Fig. 3 shows complex plane plots for the IMPS (Fig. 3a) and IMVS responses (Fig. 3b) of the full photocathode device FTO/CuI/P3HT:PCBM/TiO_2/Pt, at 0 V *vs.* RHE and under open circuit conditions, respectively (DC illumination intensity, 29.54 mW cm^{-2}; modulation of 10% of DC). Corresponding Bode plots are also shown in Fig. S5a and b (ESI†) for IMPS and IMVS data, respectively.

A detailed interpretation of the IMPS and IMVS spectra would require adequate modelling of the hybrid device, and this is beyond the goal of the present work. However, the recorded spectra allow us to gather important information about the main kinetics and expected performances of the photocathode.

First of all, we notice that both the IMPS and IMVS spectra entirely lie in the second and first quadrant, respectively, of the complex plane (*i.e.*, both photocurrent and photovoltage lag behind illumination at high frequency). IMPS spectra suggest that interface recombination processes, possibly limiting the overall PEC efficiency, are negligible, and the kinetics are instead dominated by carrier transport and extraction.[42] At low frequencies, the IMPS plot converges to a point on the real axis corresponding to the steady state photocurrent, about 229 mA W^{-1} at 28.1 Hz, which determines the actual cell conversion efficiency as the result of a balance between holes transferred to the back electrode and electrons transferred to the electrolyte. This value is consistent with the maximum photocurrent at a comparable light intensity of 530 nm, as deduced from IPCE measurements (see below). At high frequencies the modulated photocurrent tends to zero, indicating that the modulation frequency is faster than carrier transport and extraction. Importantly, it is possible to obtain a rough estimate of the average transit time τ_d for photogenerated charges from the IMPS frequency maximum:[43]

$$\tau_d = \frac{1}{2\pi \cdot f_{max}(\mathrm{IMPS})} = 0.019 \text{ ms}$$

This value is in good agreement with the ones reported for a corresponding solar cell in the literature (between 0.01 and 0.1 ms).[43,44]

Differently from IMPS, the IMVS spectra (acquired under open circuit conditions) probe the changes in the concentration of surface charges, and thus they are mainly related to interfacial recombination, *i.e.*, to an effective charge recombination time τ_{rec}:[43]

$$\tau_{rec} = \frac{1}{2\pi \cdot f_{max}(\mathrm{IMVS})} = 0.167 \text{ ms}$$

which is also in accordance with the values reported in solid solar cells (between 0.1 and 1 ms).[43,44]

Finally, the overall charge collection efficiency (η_{cc}) can be roughly estimated by:

$$\eta_{cc} = 1 - \frac{\tau_d}{\tau_{rec}} = 0.88$$

Overall, the reported data allow us to conclude that the selected photocathode architecture is expected to minimize interfacial charge recombination and to lead to good performance in terms of the extracted current, internal photon conversion efficiency and overall hydrogen evolution capability.

Photoelectrochemical characterization

Linear Sweep Voltammetry (LSV) scans were routinely performed to evaluate the onset potential (defined in this work as the potential where a cathodic photocurrent of at least 10 μA cm^{-2}

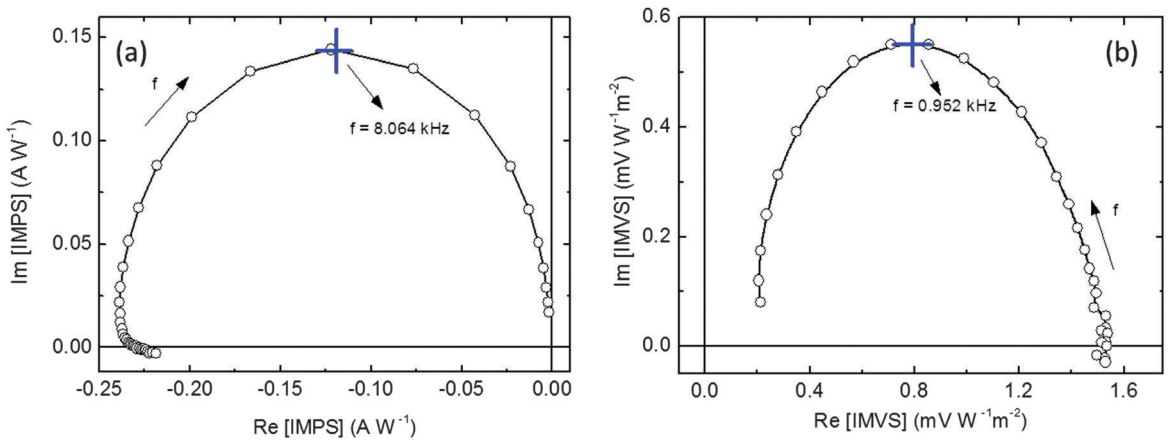

Fig. 3 IMPS (a) and IMVS (b) complex plane plots recorded at 0 V *vs.* RHE and under open circuit conditions, respectively.

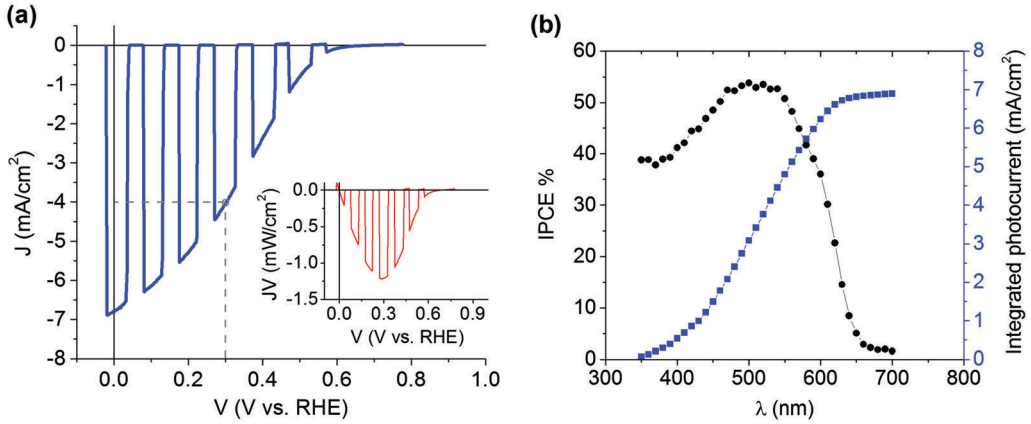

Fig. 4 Photoelectrochemical characterization in pH 1 electrolyte: (a) representative LSV scan of a hybrid photocathode under chopped light illumination (AM 1.5 G) and identification of the mpp (inset). (b) IPCE response of the hybrid photocathode at 0 V *vs.* RHE under monochromatic illumination (black trace). The photocurrent integrated over the solar spectrum is also shown (blue trace, right *Y*-axis).

is measured), the photocurrent density and the maximum power point, under simulated 1 Sun illumination (Fig. 4a). Full photocathodes exhibit high onset potentials (0.702 ± 0.007 V) *vs.* RHE and very good repeatability among replicate devices (standard deviations for figure of merit values are reported for measurements of $n = 6$ sample replicas herein). This turns into an attractive feature for further integration into a tandem photoelectrochemical cell for stand-alone water splitting. Interestingly, the onset potential seems to stabilize at 0.631 V ± 0.010 V after several LSV scans (see Fig. S6, ESI†). The photocurrent density at 0 V *vs.* RHE reaches high values as well, with a maximum recorded value of 7.10 mA cm^{-2} while averaging 6.55 ± 0.42 mA cm^{-2}. Comparable photocurrent values (up to 8 mA cm^{-2}) were previously achieved, to the best of our knowledge, only in very recent work by Jousselme and co-workers. They exploited a similar approach, but taking advantage of a buried p–n heterojunction according to the structure ITO/PEDOT:PSS/P3HT:PCBM/LiF/Al/Ti–MoS_3, thus excluding any direct liquid/semiconductor interface.[31] Another positive feature of our CuI-based hybrid photocathode is the maximum power point (mpp, defined as $d(JV)/dV = 0$), which is located at 0.303 ± 0.006 V *vs.* RHE (Fig. 4a, inset), being still positive enough to produce a photocurrent of 3.98 ± 0.01 mA cm^{-2} (as emphasized by the dashed grey line in the main panel). The mpp value is also very stable among the samples, slightly decreasing after several LSV scans to 0.269 ± 0.005 V (see Fig. S7, ESI†).

The Incident Photon-to-Current Efficiency (IPCE) is a valuable diagnostic figure of merit for PEC devices. Fig. 4b shows an IPCE value higher than 50% at the maximum wavelength absorption of the photoactive layer, around 500 nm. This indicates that half of the photons impinging over the photocathode between wavelengths 450 and 550 nm are converted into electrons capable of driving redox reactions (likely the HER) at the catalyst/electrolyte interface. This IPCE value is, to the best of our knowledge, superior to any other P3HT-based organic photocathode previously reported. Importantly, the integrated photocurrent (6.90 mA cm^{-2}, blue line) extracted from the IPCE data, matches well with the value measured by the LSV.

In order to disentangle the specific contributions of the hole selective, the electron selective and the catalyst layers to the overall performances of the hybrid photocathode, we realized complementary devices by removing from the architecture one component at a time (Fig. 5). The analysis of the curves shown indicates that the hole selective CuI layer clearly has the greatest impact on the increase in photovoltage towards highly positive potential, while the TiO_2 layer aids in reducing carrier recombination and enhances electron collection towards the electrocatalyst; thus synergistically improving both the photocurrent and mpp. This is clearly noticed from the cases without the CuI layer and without the TiO_2 one. In the former case, photocurrents lower than 100 μA cm^{-2} are obtained at 0 V *vs.* RHE while the onset potential lies at 0.171 V *vs.* RHE. For the latter case, 1.5 mA cm^{-2} of photocurrent is produced at 0 V *vs.* RHE while the onset potential is at 0.372 V *vs.* RHE. The importance of the presence of an active catalyst for hydrogen evolution is also clear, as the photocurrent density only reaches 600 μA cm^{-2} at 0 V *vs.* RHE (gray trace) when Pt is missing, although the onset potential is comparable to the case of the full device (0.603 V). Besides, the photocurrent transient dynamics observed during light chopping indicates a significant charge accumulation of capacitive nature, due to less efficient carrier extraction at the TiO_2/electrolyte interface.

Stability tests under potentiostatic conditions were performed at 0 V *vs.* RHE and the photocurrent was recorded under continuous simulated AM 1.5G illumination (Fig. 5a). Chronoamperometry (CA) data show an average initial photocurrent value of 7.42 ± 1.43 mA cm^{-2} (maximum recorded value, 8.29 mA cm^{-2}) followed by a steep decrease in performance down to 3.00 ± 0.13 mA cm^{-2} during the first 20 minutes (photocurrent loss by ~60%, vertical double arrows). After 1 hour of continuous operation, the photocurrent density reaches 1.31 ± 0.13 mA cm^{-2}. Afterwards, a LSV scan was run confirming the photocurrent.

In order to confirm the light-assisted evolution of hydrogen, gas chromatography (GC) measurements were carried out. The recorded CA curve (Fig. 6b, red trace) shows that the initial

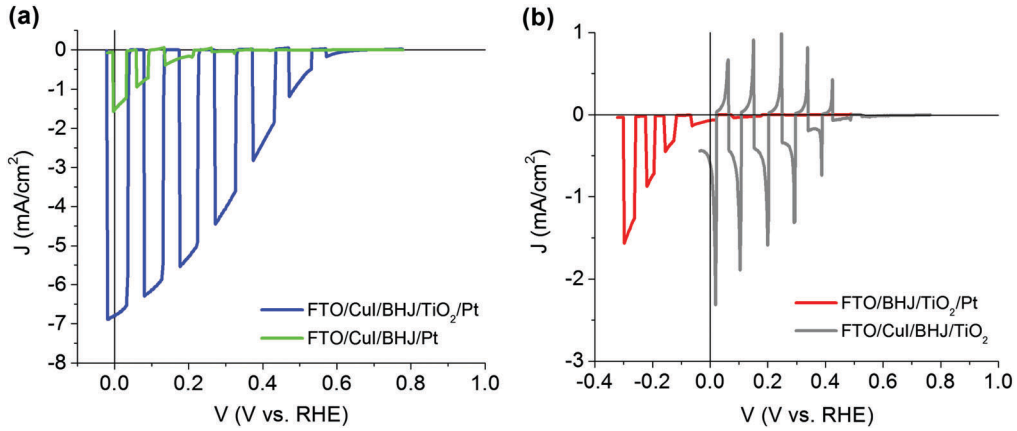

Fig. 5 Comparison between hybrid photocathodes with full and partial architectures. LSV scans at pH 1 under chopped light illumination (AM 1.5 G): (a) full device shown for comparison (blue trace) and device lacking only the TiO_2 layer (green trace). (b) Device lacking only the CuI layer (red trace) and device without the Pt layer (gray trace).

photocurrent density (8.22 mA cm^{-2}) decreases down to 3.91 mA cm^{-2} after 20 minutes of operation, decaying finally to 2.1 mA cm^{-2} after one hour. Although this shows a similar trend to the measurements reported in Fig. 5, in this case, the temporal stability appears to be slightly improved. This may be due to the fact that oxygen was generated at the counter electrode contained in a separated compartment, to avoid cross-over during gas collection. Indeed, the presence of dissolved oxygen in the electrolyte may play a role in the latter stage of photocathode operation, when its inner layers are more exposed to the electrolyte after partial Pt delamination (see the results below). The amount of hydrogen detected at each sampling point was converted to its equivalent faradaic current, producing the trend shown in Fig. 6b, which matches very well with the trend of the CA. The faradaic efficiency was calculated at each point, producing an average value of 100 ± 5%. Accordingly, we can safely conclude that our hybrid organic/inorganic photocathode produces hydrogen with a faradaic efficiency of 100%.

Implementation of a protective coating

The device was shown to produce hydrogen at high yield, even following an initial decline in photocurrent density, indicating the deactivation of some of its components. Hence, we inspected the device after CA stability tests. The photocathode surface (Fig. 7) clearly shows large areas where Pt delamination occurs (panel a) (scanned area of 800 × 550 μm^2), exposing the underneath TiO_2 layer to the electrolyte. Micron-sized fractures, produced during the thermal annealing of the device as the last step of fabrication, are clearly visible (Fig. 7a and Fig. S8, ESI†). These fractures appear as a consequence of the mismatch between the thermal expansion coefficient of the organic material and the oxide layer.[45] Evaluating the material morphology at a smaller scale (Fig. 5b) allows to appreciate the nanoporous structure of the exposed TiO_2, in close correspondence to delaminated and folded back fragments of Pt (Fig. 7b and Fig. S9, ESI†). In order to further support the role of Pt detachment in the degradation in the performance of stressed photocathodes, we attempted to

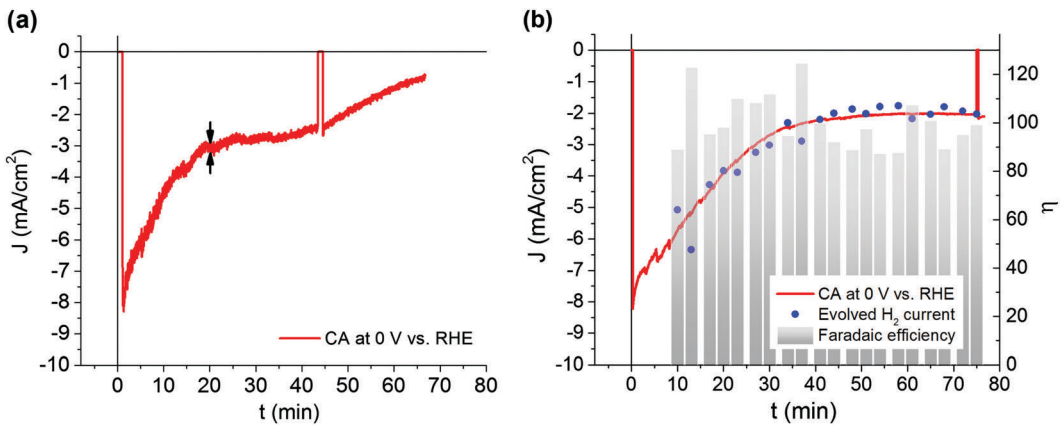

Fig. 6 Potentiostatic stability tests of hybrid photocathodes at pH 1 and 0 V *vs.* RHE under simulated illumination AM 1.5 G. (a) Representative initial CA run lasting 4000 s (the vertical double arrows mark the ~60% loss of photocurrent). Dark current was monitored eventually. (b) CA run (red trace) during periodic measurement of evolved hydrogen by GC (blue dots). The calculated faradaic efficiency is also shown (gray columns, right *Y*-axis).

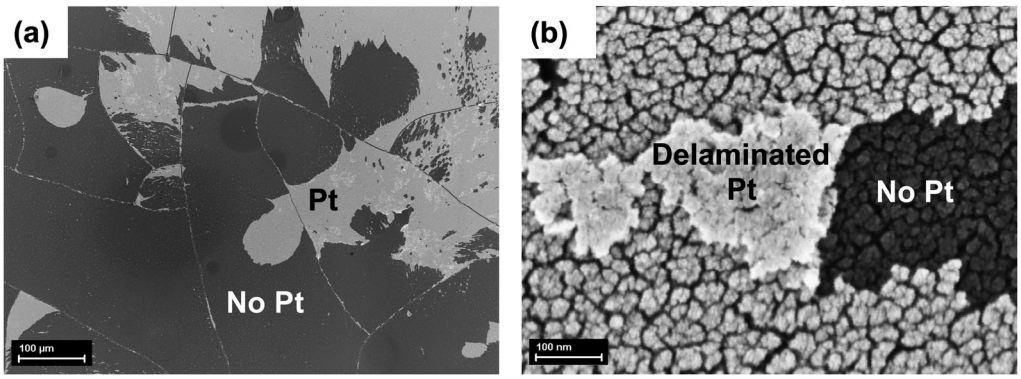

Fig. 7 SEM micrographs of the surface (capping Pt layer on top of the nanostructured TiO_2) of a hybrid photocathode. (a) View of the surface after one hour operation at 0 V *vs.* RHE, pH 1 and 1 sun illumination (scale bar 100 μm). (b) HR-SEM magnification showing Pt delamination and fragments folded back (scale bar 100 nm).

quantify the fraction of photocurrent recovery after a second catalyst deposition (re-platinization). This illustrative experiment is described in the ESI† (Fig. S10), and clearly shows a recovery in the photocurrent to a significant extent.

It has been reported that Pt on TiO_2 is prone to detachment following operation in acid.[46] Catalyst delamination might further worsen as a consequence of sustained photocurrent flowing in the device, thus possibly explaining the quick, initial degradation of performance upon illumination. Based on these observations, we developed a protective layer intended to prevent catalyst dislodging and to stabilize the overall performance of the hybrid photocathode. Actually, this is not an easy task, since the material of choice should not fully isolate the catalyst from the electrolyte, being permeable enough to allow efficient hydrogen evolution. Moreover, the processing conditions must be compatible with the underlying layers, and the coating must be stable in an aqueous environment. The material of choice here is the branched polymer polyethyleneimine (PEI), due to its good adhesion and coating properties,[47] hydrophilicity, proton affinity[48] and chelating properties on both ions[49] and metals.[50] A solution-processed overlayer of PEI is thus expected to minimize the Pt dislodging, however without hindering the electrocatalytic activity, and consequently limiting to some extent the electrolyte permeation towards the inner layers. Ethanol proved to be a good solvent for PEI solution preparation, due to its good wettability over the surface of the photocathode. A suitable solution concentration was found to be around 0.1% in weight, whereas higher concentrations produce films that hindered the catalyst activity. LSV scans before and after the stability tests are shown in Fig. 8.

The LSV scan shows that neither the onset potential, the photocurrent density at 0 V *vs.* RHE or the mpp are negatively affected by the PEI over-layer on top of the platinum catalyst (0.715 ± 0.013 V, 6.80 mA cm^{-2} and 0.315 ± 0.007 V respectively) (Fig. 8a). The CA test reveals that the photocurrent decrease over time still occurs, but at a significantly lower rate (Fig. 8b). Indeed, ~60% of the photocurrent loss, as observed in Fig. 6a, is delayed more than two-fold, now occurring after 50 minutes (vertical double arrows in panel b). From this moment onwards and towards the end of the CA, the photocurrent remains stable

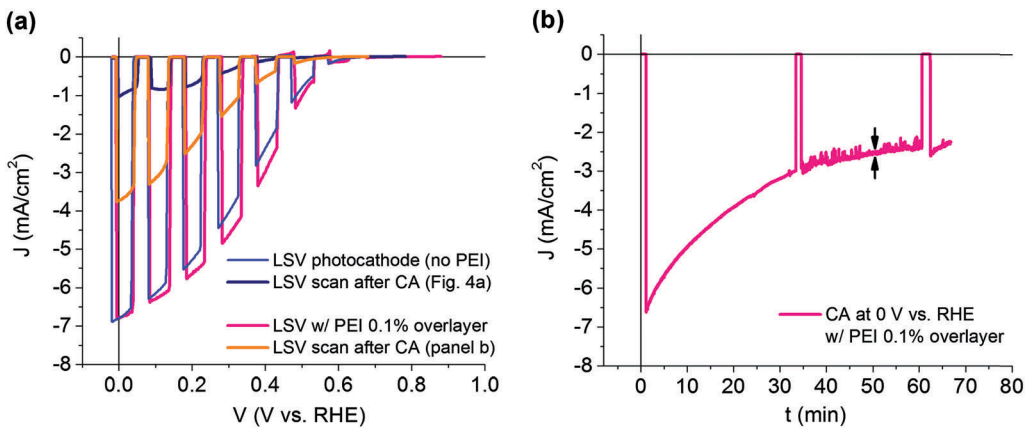

Fig. 8 Effect of the PEI over-layer on the photoelectrochemical behavior of a hybrid photocathode at pH 1 and AM 1.5 illumination: (a) LSV scan under chopped light of photocathode protected with an over-layer of PEI 0.1% (pink trace) as compared to the device without this overlayer (blue trace). The LSV scans performed after the CA run on each type of device are also shown (PEI: orange trace and no PEI: blue navy trace). (b) CA test at 0 V *vs.* RHE of the protected photocathode.

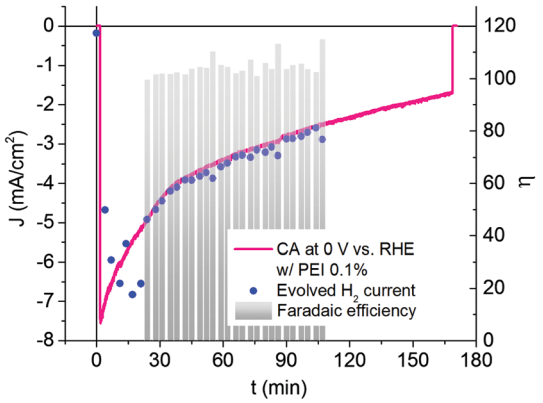

Fig. 9 Hydrogen detection from a hybrid photocathode protected with an over-layer of PEI 0.1%. Extended CA at 0 V *vs.* RHE, pH 1 and simulated illumination AM 1.5 G (pink trace), during periodic measurement of evolved hydrogen by GC (blue dots). The calculated faradaic efficiency is also shown (gray columns, right *Y*-axis).

around 2.40 mA cm^{-2}. In addition, the LSV scan performed after the CA test exhibits a clear superior performance, in terms of photocurrent, mpp and stability, over the one recorded after the CA in the uncoated photocathode. Particularly, the photocurrent density at 0 V *vs.* RHE amounts now to 3.73 mA cm^{-2} against 1.01 mA cm^{-2} for the pristine photocathode. Interestingly, the onset potential recorded after the CA is in both cases essentially equal to 0.58 V (0.582 ± 0.003 V *vs.* 0.579 ± 0.003 V, respectively). In contrast, an improvement in the mpp clearly occurs due to the positive effect of the PEI coating on the temporal behaviour of such devices, lying now at 0.212 ± 0.006 V.

GC measurements on photocathodes protected by the PEI overlayer, under the same conditions as those used for pristine photocathodes, are shown in Fig. 9. As before, the faradaic current corresponding to the amount of hydrogen gas detected at each GC sampling point matches very well with the experimental CA trend. An average faradaic efficiency of 104.7 ± 1.5% is obtained, thus confirming 100% yield for hydrogen generation by the hybrid photocathode in the presence of the PEI protective coating. Interestingly, the GC measurements are less dispersed than in the non-protected case. Overall, the use of the PEI coating allowed us to considerably extend the operational time of the hybrid photocathode, ending up by generating 1.68 mA cm^{-2} at 0 V *vs.* RHE after three hours of continuous functioning upon 1 sun illumination under acidic conditions. In general, a stabilization of the relevant parameters discussed above is observed in the presence of PEI coating.

Discussion

A careful selection of suitable charge selective layers is of paramount importance in PEC technology, since it governs the main figures of merit of the final device, the onset potential, photocurrent density and maximum power point. Focusing on the hole selective layer, CuI as a substitute for the typical PEDOT:PSS and for the more recent MoO_3[33] exhibits favourable matching to the energetic levels of the organic semiconductor, compatibility with the subsequent deposition of the conjugated polymer blend and the capability to sustain the final thermal annealing treatment. In addition, it is a solution-processable material and also transparent. Our work demonstrates that CuI is able to satisfy all these requirements, introducing significant advantages over other hole selective layers and contributing notably to the competitive performance of the hybrid photocathode here reported.

As shown above, the CuI layer contributes the most to the value of the onset potential obtained for this polymer-based photocathode. Onset potential values larger than 0.6 V are uncommon even among state-of-the-art inorganic photocathodes, only surpassed by recent improvements in a-Si,[11b] CIGS[51] and Cu_2O[52] with values between 0.9 and 1 V *vs.* RHE. In the case of photocathodes based on conjugated polymers, interesting values were reported only in one recent study by Loi and co-workers, based on a type II heterojunction CdSe:P3HT (0.85 V *vs.* RHE). In that case, however, photocurrent densities were considerably lower (1.5 mA cm^{-2} at 0 V *vs.* RHE, pH 7).[30] Moreover, we noticed that the stability of the onset potential is rarely discussed in the literature, so it is not straightforward making direct comparisons between the CuI-based photocathode and similar, hybrid systems. In our case, however, the onset potential exhibits a tendency towards stability. The fact that the onset potential is characterized by good stability, while the photocurrent is not, prompted us to look for major causes of device instability in the outer layers of the device.

TiO_2 is considered to be a stable compound under air and aqueous conditions exhibiting a wide potential-pH window over the entire pH range, although narrower in potential around pH 1 but stable still as long as it remains more positive than −0.4 V *vs.* RHE (see the Pourbaix diagram of Ti, ref. 53). Despite the benefits in photocathode performance by using the as-prepared hierarchical nanostructured titania as the electron selective layer (Fig. 3), its mesoporous character leads to some concerns regarding the physical integrity of the device, as the electrolyte may permeate the inner layers. This has been discussed previously within the context of the MoO_3-based hybrid photocathode, which actually requires such ion intercalation to achieve top performance, although turning detrimental upon extended operation.[33] Electrolyte permeation might be avoided in the future by either migrating to a thicker earth-abundant HER catalyst and/or a conformal titania layer. With the aim to realize the latter, we are currently following different approaches: dense TiO_2 by PLD, sol–gel and atomic layer deposition methods. Here, however, we intentionally focused our attention on a more relevant problem, catalyst delamination.

The use of a PEI protective coating represents a very simple, yet original and promising strategy. Our results clearly indicate that a thin PEI layer protects the photocathode, while neither disrupting the electrocatalytic activity nor introducing new issues in photocathode overall performances. We also notice that the GC measurements after the first 20 minutes are considerably less dispersed in the case of the protected device than in the non-protected one. Interestingly, we also noted that the PEI surface remained almost free of accumulating hydrogen

bubbles during photocathode operation. Conversely, on the exposed Pt surface in the non-protected device the bubbles formed and grew over time remaining well attached to the surface, thus representing a common issue experienced in catalytic gas generation.[54] Overall, the improvement in the photocathode performances offered by the PEI overlayer, even though still far from being optimized, is promising, and allows the photocathode to continuously operate for almost three hours ending up on 1.68 mA cm^{-2} at 0 V *vs.* RHE.

Finally, the solar to hydrogen efficiency (STH) in a two-electrode configuration at zero bias under standard AM 1.5 G illumination is the ultimate benchmark efficiency regarding solar-to-fuel conversion.[2] However, a practical figure of merit for photoelectrodes is the power saved P_{saved}, understood as the ability (voltage) of the photoelectrode to drive the fuel evolution reaction at a certain current, with respect to the voltage needed for a selected dark electrode to maintain the same current. When P_{saved} is referenced to the power solar input P_s, the ratiometric power saved Φ_{saved} is obtained.[55] For the case of the hydrogen evolution reaction driven by a photocathode at its maximum power point (mpp) with respect to an ideally non-polarizable dark electrode (*i.e.* the RHE, with $V_{RHE} = 0$ at any current), the ideal ratiometric power-saving figure of merit is:

$$\Phi_{saved,ideal} = J_{mpp}(V_{mpp} - V_{RHE})/P_s = J_{mpp}\cdot V_{mpp}/P_s$$

In our case (J_{mpp} = 3.98 mA cm^{-2}, V_{mpp} = 0.303 V *vs.* RHE, P_s = 100 mW cm^{-2}), the ideal ratiometric power saved is equal to 1.21%. This figure of merit allows direct comparisons between disparate systems and measurements. Taking as reference the recent photocathode reported by Jousselme and co-workers (ITO/PEDOT:PSS/P3HT:PCBM/LiF/Al/Ti–catalyst), the obtained $\Phi_{saved,ideal}$ is 0.64% for the MoS_3 catalyst, while it is 1.18% for the Pt–C one.[31] In that case, differences arise due to the over-potentials required to drive the HER at such currents, thus depending on the catalyst used; with Pt–C a better catalyst as expected. Notice that in our case, by using a simpler architecture we have achieved comparable results, enabling further optimization of the photocathode. The calculation of the $\Phi_{saved,ideal}$ for the PEI-protected photocathode leads to a value equal to 1.45% (J_{mpp} = 4.61 mA cm^{-2}, V_{mpp} = 0.315 V *vs.* RHE, P_s = 100 mW cm^{-2}). The factor that contributes the most to this enhancement is the increment in photocurrent at the mpp.

Conclusions

In conclusion, we have presented a hybrid photocathode for solar hydrogen production, with the architecture FTO/CuI/P3HT:PCBM/TiO_2/Pt, working under acidic aqueous electrolyte conditions and simulated 1 sun illumination. As novel features with respect to previous related photocathodes, we have introduced solution-processable cuprous iodide (CuI) as the anode layer, a nanostructured porous TiO_2 layer as the electron selective layer and a polyethyleneimine (PEI) protective coating. By depositing a CuI solution-based hole selective layer without any further thermal annealing, we have shown clear advantages in terms of performance, stability and scalability with respect to the prototypical PEDOT:PSS anode layer used in previous studies. The high onset potential achieved here is attributable to the use of CuI as the hole selective layer. Also, the growth of a nanoporous hierarchical TiO_2 layer on top of the polymer–fullerene bulk heterojunction boosts the photocurrent and mpp, due to efficient electron collection and transport to the Pt catalyst, as supported also by non-steady state spectroscopy measurements, carried out under the very same operating conditions of the photocathode. These improvements lead to the achievement of photocurrents as high as 8 mA cm^{-2} at 0 V *vs.* RHE, an onset potential for the HER equal to 0.702 V as well as a maximum power point located at 0.303 V, which illustrate clear advantages of the approach herein reported. As a consequence, the achievement of 100% faradaic efficiency during hydrogen evolution, an IPCE above 50% and an ideal ratiometric power-saving figure of merit equal to 1.21% showed superior performance against competitive photocathodes. However, platinum detachment during photocathode operation leads to a detrimental performance over a one hour time span, although maintaining 100% faradaic efficiency for the HER throughout the test. The novel PEI over-coating clearly illustrates the potential of this simple approach to ultimately stabilize the photocathode performance. Further improvements will target a further stabilized photocathode performance and the use of earth-abundant catalysts. The use of alternative efficient polymer–fullerene donor–acceptor blends tailored toward the water splitting reaction may also boost the photocathode performance and efficiency. Ultimately, these results demonstrate the viability of using conjugated polymer-based photocathodes for efficient hydrogen generation, with potential for integration into tandem photoanode–photocathode or PV-biased-photocathode configurations. The ultimate goal, from a scalability point of view, of an all-solution processed hydrogen evolving photocathode can be also foreseen.

Acknowledgements

Funding. This work was supported by the EU through the Future and Emerging Technologies (FET) programme under the FP7, Collaborative Project 309223 (PHOCS, Photogenerated Hydrogen by Organic Catalytic Systems). **Author contributions**. H. C. and S. B. fabricated the devices, helped by G. T., and carried out electrochemical characterization, with help from S. L. F. F. deposited the TiO_2 and the catalyst layers. M. T. M. and M. S. carried out GC and IPCE measurements. F. D. F. took care of SEM analysis. F. D. F. and M. R. A. planned and supervised the work. All authors contributed to the interpretation of the results and manuscript drafting. **Competing interests**. The authors declare that they have no competing interests.

Notes and references

1 (*a*) R. van de Krol and M. Grätzel, in *Photoelectrochemical Hydrogen Production*, ed. R. van de Krol and M. Grätzel, Springer, New York, 2012, pp. 3–11; (*b*) J. P. Holdren, Energy and sustainability, *Science*, 2007, **315**, 737.

2 Z. Chen, H. N. Dinh and E. Miller, *Photoelectrochemical Water Splitting. Standards, Experimental Methods and Protocols*, Springer, New York, 2013, pp. 1–5.

3 *Basic Research Needs for Solar Energy Utilization*, ed. N. S. Lewis and G. Crabtree, Office of Science, US Department of Energy, Washington, DC, 2005, pp. 3–10.

4 (*a*) J. R. Bolton, S. J. Strickler and J. S. Connolly, Limiting and realizable efficiencies of solar photolysis of water, *Nature*, 1985, **316**, 495–500; (*b*) L. C. Seitz, Z. Chen, A. J. Forman, B. A. Pinaud, J. D. Benck and T. F. Jaramillo, Modeling practical performance limits of photoelectrochemical water splitting based on the current state of materials research, *ChemSusChem*, 2014, **7**, 1372–1385.

5 B. A. Pinaud, J. D. Benck, L. C. Seitz, A. J. Forman, Z. Chen, T. G. Deutsch, B. D. James, K. N. Baum, G. N. Baum, S. Ardo, H. Wang, E. Miller and T. F. Jaramillo, Technical and economic feasibility of centralized facilities for solar hydrogen production *via* photocatalysis and photoelectrochemistry, *Energy Environ. Sci.*, 2013, **6**, 1983–2002.

6 (*a*) O. Khaselev and J. A. Turner, A Monolithic Photovoltaic-Photoelectrochemical Device for Hydrogen Production *via* Water Splitting, *Science*, 1998, **280**, 425–427; (*b*) O. Khaselev, A. Banasal and J. A. Turner, High-efficiency integrated multijunction photovoltaic/electrolysis systems for hydrogen production, *Int. J. Hydrogen Energy*, 2001, **26**, 127–132.

7 M. M. May, H.-J. Lewerenz, D. Lackner, F. Dimroth and T. Hannappel, Efficient direct solar-to-hydrogen conversion by *in situ* interface transformation of a tandem structure, *Nat. Commun.*, 2015, **6**, 8286.

8 S. Licht, B. Wang, S. Mukerji, T. Soga, M. Umeno and H. Tributsch, Over 18% solar energy conversion to generation of hydrogen fuel; theory and experiment for efficient solar water splitting, *Int. J. Hydrogen Energy*, 2001, **26**, 653–659.

9 J. Luo, J.-H. Im, M. T. Mayer, M. K. Nazeeruddin, N. G. Park, S. D. Tilley, H. J. Fan and M. Grätzel, Water photolysis at 12.3% efficiency *via* perovskite photovoltaics and Earth-abundant catalysts, *Science*, 2014, **345**, 1593–1596.

10 M. G. Walter, E. L. Warren, J. R. McKone, S. W. Boettcher, Q. Mi, E. A. Santori and N. S. Lewis, Solar water splitting cells, *Chem. Rev.*, 2010, **110**, 6446–6463.

11 (*a*) S. Y. Reece, J. A. Hamel, K. Sung, T. D. Jarvi, A. J. Esswein, J. J. H. Pijpers and D. G. Nocera, Wireless Solar Water Splitting Using Silicon-Based Semiconductors and Earth-Abundant Catalysts, *Science*, 2011, **334**, 645–648; (*b*) Y. Lin, C. Battaglia, M. Boccard, M. Hettick, Y. Zhibin, B. Christophe, J. W. Ager and A. Javey, Amorphous Si thin film based photocathodes with high photovoltage for efficient hydrogen production, *Nano Lett.*, 2013, **13**, 5615–5618.

12 (*a*) S. S. Kocha and J. A. Turner, Displacement of the Band-edges of $GaInP_2$ in Aqueous Electrolytes Induced by Surface Modification, *J. Electrochem. Soc.*, 1995, **142**, 2625–2630; (*b*) M. H. Lee, K. Takei, J. Zhang, R. Kapadia, M. Zheng, Y. Z. Chen, J. Nah, T. S. Matthews, Y. L. Chueh, J. W. Ager and A. Javey, p-Type InP Nanopillar Photocathodes for Efficient Solar-Driven Hydrogen Production, *Angew. Chem., Int. Ed.*, 2012, **51**, 10760–10764.

13 (*a*) H. Kumagai, T. Minegishi, N. Sato, T. Yamada, J. Kubota and K. Domen, Efficient Solar Hydrogen Production from Neutral Electrolytes Using Surface-Modified $Cu(In,Ga)Se_2$ Photocathodes, *J. Mater. Chem. A*, 2015, **3**, 8300–8307; (*b*) B. J. Li, P. F. Yin, Y. Z. Zhou, Z.-M. Gao, T. Ling and X.-W. Du, Single crystalline Cu_2ZnSnS_4 nanosheet arrays for efficient photochemical hydrogen generation, *RSC Adv.*, 2015, **5**, 2543–2549.

14 (*a*) A. Paracchino, N. Mathews, T. Hisatomi, M. Stefik, S. D. Tilley and M. Grätzel, Ultrathin films on copper(I) oxide water splitting photocathodes: a study on performance and stability, *Energy Environ. Sci.*, 2012, **5**, 8673–8681; (*b*) J. Azevedo, L. Steier, P. Dias, M. Stefik, C. T. Sousa, P. Araujo, A. Mendes, M. Grätzel and S. D. Tilley, On the stability enhancement of cuprous oxide water splitting photocathodes by low temperature steam annealing, *Energy Environ. Sci.*, 2014, **7**, 4044–4052; (*c*) C. G. Morales-Guio, L. Liardet, M. T. Mayer, S. D. Tilley, M. Grätzel and X. Hu, Photoelectrochemical Hydrogen Production in Alkaline Solutions Using Cu_2O Coated with Earth-Abundant Hydrogen Evolution Catalysts, *Angew. Chem., Int. Ed.*, 2015, **54**, 664–667.

15 N. K. Awad, E. A. Ashour and N. K. Allam, Recent advances in the use of metal oxide-based photocathodes for solar fuel production, *J. Renewable Sustainable Energy*, 2014, **6**, 022702.

16 J. You, L. Dou, K. Yoshimura, T. Kato, K. Ohya, T. Moriarty, K. Emery, C.-C. Chen, J. Gao, G. Li and Y. Yang, A polymer tandem solar cell with 10.6% power conversion efficiency, *Nat. Commun.*, 2013, **4**, 1446–1456.

17 M. A. Green, K. Emery, Y. Hishikawa, W. Warta and E. D. Dunlop, Solar cell efficiency tables (Version 45), *Prog. Photovoltaics*, 2015, **23**, 1–9.

18 (*a*) A. Facchetti, π-Conjugated Polymers for Organic Electronics and Photovoltaic Cell Applications, *Chem. Mater.*, 2011, **23**, 733–758; (*b*) R. S. Sprick, J.-X. Jiang, B. Bonillo, S. Ren, T. Ratvijitvech, P. Guiglion, M. A. Zwijnenburg, D. J. Adams and A. I. Cooper, Tunable Organic Photocatalysts for Visible-Light-Driven Hydrogen Evolution, *J. Am. Chem. Soc.*, 2015, **137**, 3265–3270.

19 (*a*) F. C. Krebs, Processing and preparation of polymer and organic solar cells, *Sol. Energy Mater. Sol. Cells*, 2009, **93**, 394; (*b*) M. Caironi and Y. Y. Noh, *Large area and flexible electronics*, John Wiley and Sons, New York, 2015.

20 (*a*) M. O. Reese, A. J. Morfa, M. S. White, N. Kopidakis, S. E. Shaheen, G. Rumbles and D. S. Ginley, Pathways for the degradation of organic photovoltaic P3HT:PCBM based devices, *Sol. Energy Mater. Sol. Cells*, 2008, **92**, 746–752; (*b*) T. S. Glen, N. W. Scarratt, H. Yi, A. Iraqi, T. Wang, J. Kingsley, A. R. Buckley, D. G. Lidzey and A. M. Donald, Grain size dependence of degradation of aluminium/calcium cathodes in organic solar cells following exposure to humid air, *Sol. Energy Mater. Sol. Cells*, 2015, **140**, 25–32.

21 S. Hu, N. S. Lewis, J. W. Ager, J. Yang, J. R. McKone and N. C. Strandwitz, Thin-Film Materials for the Protection of Semiconducting Photoelectrodes in Solar-Fuel Generators, *J. Phys. Chem. C*, 2015, **119**, 24201–24228.

22 S. Esiner, H. van Eersel, M. M. Wienk and R. A. J. Janssen, Triple Junction Polymer Solar Cells for Photoelectrochemical Water Splitting, *Adv. Mater.*, 2013, **25**, 2932–2936.

23 J. Luo, Z. Li, S. Nishiwaki, M. Schreier, M. T. Mayer, P. Cendula, Y. H. Lee, K. Fu, A. Cao, M. K. Nazeeruddin, Y. E. Romanyuk, S. Buecheler, S. D. Tilley, L. H. Wong, A. N. Tiwari and M. Grätzel, Targeting Ideal Dual-Absorber Tandem Water Splitting Using Perovskite Photovoltaics and $CuIn_xGa_{1-x}Se_2$ Photocathodes, *Adv. Energy Mater.*, 2015, **5**, 1501520.

24 (*a*) S. Bellani, D. Fazzi, P. Bruno, E. Giussani, E. V. Canesi, G. Lanzani and M. R. Antognazza, Reversible P3HT/Oxygen Charge Transfer Complex Identification in Thin Films Exposed to Direct Contact with Water, *J. Phys. Chem. C*, 2014, **118**, 6291–6299; (*b*) M. R. Antognazza, D. Ghezzi, D. Musitelli, M. Garbugli and G. Lanzani, A hybrid solid-liquid polymer photodiode for the bioenvironment, *Appl. Phys. Lett.*, 2009, **94**, 243501.

25 G. Dennler, M. C. Scharber and C. J. Brabec, Polymer-Fullerene Bulk-Heterojunction Solar Cells, *Adv. Mater.*, 2009, **21**, 1323–1338.

26 (*a*) O. Winther-Jensen, B. Winther-Jensen and D. R. MacFarlane, Photostimulated electrocatalysis of water oxidation by conjugated polymers, *Electrochem. Commun.*, 2011, **13**, 307–309; (*b*) O. A. El-Rashiedy and S. Holdcroft, Photoelectrochemical Properties of Poly(3-alkylthiophene) Films in Aqueous Solution, *J. Phys. Chem.*, 1996, **100**, 5481–5484; (*c*) G. Suppes, E. Ballard and S. Holdcroft, Aqueous photocathode activity of regioregular poly(3-hexylthiophene), *Polym. Chem.*, 2013, **4**, 5345–5351; (*d*) C. Hin Ng, C. A. Ohlin, S. Qiu, C. Sun and B. Winther-Jensen, Mechnaistic studies of the photo-electrochemical hydrogen evolution reaction on poly(2-2'-bithiophene), *Catal. Sci. Technol.*, 2016, **6**, 3253.

27 (*a*) E. Lanzarini, M. R. Antognazza, M. Biso, A. Ansaldo, L. Laudato, P. Bruno, P. Metrangolo, G. Resnati, D. Ricci and G. Lanzani, Polymer-Based Photocatalytic Hydrogen Generation, *J. Phys. Chem. C*, 2012, **116**, 10944–10949; (*b*) T. Bourgeteau, D. Tondelier, B. Geffroy, R. Brisse, C. Laberty-Robert, S. Campidelli, R. de Bettignies, V. Artero, S. Palacin and B. Jousselme, A H_2-evolving photocathode based on direct sensitization of MoS_3 with an organic photovoltaic cell, *Energy Environ. Sci.*, 2013, **6**, 2706–2713; (*c*) M. P. Gustafson, N. Clark, B. Winther-Jensen and D. R. MacFarlane, Organic Photovoltaic Structures as Photo-active Electrodes, *Electrochim. Acta*, 2014, **140**, 309–313.

28 M. Haro, C. Solis, G. Molina, L. Otero, J. Bisquert, S. Gimenez and A. Guerrero, Toward Stable Solar Hydrogen Generation Using Organic Photoelectrochemical Cells, *J. Phys. Chem. C*, 2015, **119**, 6488–6494.

29 A. Guerrero, M. Haro, S. Bellani, M. R. Antognazza, L. Meda, S. Gimenez and J. Bisquert, Organic photoelectrochemical cells with quantitative photocarrier conversion, *Energy Environ. Sci.*, 2014, **7**, 3666–3673.

30 L.-H. Lai, W. Gomulya, M. Berghuis, L. Protesescu, R. J. Detz, J. N. H. Reek, M. V. Kovalenko and M. A. Loi, Organic–Inorganic Hybrid Solution-Processed H_2-Evolving Photocathodes, *ACS Appl. Mater. Interfaces*, 2015, **7**, 19083–19090.

31 T. Bourgeteau, D. Tondelier, B. Geffroy, R. Brisse, R. Cornut, V. Artero and B. Jousselme, Enhancing the Performances of P3HT:PCBM–MoS_3-Based H_2-Evolving Photocathodes with Interfacial Layers, *ACS Appl. Mater. Interfaces*, 2015, **7**, 16395–16403.

32 (*a*) S. R. Dupont, M. Oliver, F. C. Krebs and R. H. Dauskardt, Interlayer adhesion in roll-to-roll processed flexible inverted polymer solar cells, *Sol. Energy Mater. Sol. Cells*, 2012, **97**, 171–175; (*b*) K. Norrman, M. V. Madsen, S. A. Gevorgyan and F. C. Krebs, Degradation patterns in water and oxygen of an inverted polymer solar cell, *J. Am. Chem. Soc.*, 2010, **132**, 16883–16892.

33 F. Fumagalli, S. Bellani, M. Schreier, S. Leonardi, H. Comas Rojas, A. Ghadirzadeh, G. Tullii, A. Savoini, G. Marra, L. Meda, M. Grätzel, G. Lanzani, M. T. Mayer, M. R. Antognazza and F. Di Fonzo, Hybrid organic–inorganic H_2-evolving photocathodes: understanding the route towards high performance organic photoelectrochemical water splitting, *J. Mater. Chem. A*, 2016, **4**, 2178–2187.

34 (*a*) W. Sun, H. Peng, Y. Li, W. Yan, Z. Liu, Z. Bian and C. Huang, Solution-Processed Copper Iodide as an Inexpensive and Effective Anode Buffer Layer for Polymer Solar Cells, *J. Phys. Chem. C*, 2014, **118**, 16806–16812; (*b*) Y. Peng, N. Yaacobi-Gross, A. K. Perumal, H. A. Faber, G. Vourlias, P. A. Patsalas, D. D. C. Bradley, Z. He and T. D. Anthopoulos, Efficient organic solar cells using copper(I) iodide (CuI) hole transport layers, *Appl. Phys. Lett.*, 2015, **106**, 243302.

35 M. Grundmann, F.-L. Schein, M. Lorenz, T. Böntgen, J. Lenzner and H. von Wenckstern, Cuprous iodide – a p-type transparent semiconductor: history and novel applications, *Phys. Status Solidi A*, 2013, **210**, 1671–1703.

36 L. Passoni, L. Criante, F. Fumagalli, F. Scotognella, G. Lanzani and F. Di Fonzo, Self-Assembled Hierarchical Nanostructures for High-Efficiency Porous Photonic Crystals, *ACS Nano*, 2014, **8**, 12167–12174.

37 A. Luzio, F. G. Ferré, F. D. Fonzo and M. Caironi, Hybrid Nanodielectrics for Low-Voltage Organic Electronics, *Adv. Funct. Mater.*, 2014, **24**, 1790–1798.

38 B. A. Boukamp, *J. Electrochem. Soc.*, 1995, **142**, 1885–1894.

39 S. Shao, J. Liu, J. Zhang, B. Zhang, Z. Xie, Y. Geng and L. Wang, Interface-Induced Crystalline Ordering and Favorable Morphology for Efficient Annealing-Free Poly(3-hexylthiophene): Fullerene Derivative Solar Cells, *ACS Appl. Mater. Interfaces*, 2012, **4**, 5704–5710.

40 (*a*) S. Das, J.-Y. Choi and T. L. Alford, P3HT:PC_{61}BM based solar cells employing solution processed copper iodide as the hole transport layer, *Sol. Energy Mater. Sol. Cells*, 2015, **133**, 255–259; (*b*) S. Yoon, H. Kim, E.-Y. Shin, Y.-Y. Noh, B. Park and I. Hwang, Thickness dependence of a CuI hole transport layer on initial photostability and photovoltaic performance of organic solar cells, *Phys. Status Solidi A*, 2016, 1–7.

41 (*a*) E. A. Ponomarev and L. M. Peter, *J. Electroanal. Chem.*, 1995, **396**, 219–226; (*b*) J. E. Thorne, J.-W. Jang, E. Y. Liu and D. Wang, *Chem. Sci.*, 2016, **7**, 3347–3354.

42 H. K. Dunn, J. M. Feckl, A. Muller, D. Fattakhova-Rohlfing, S. G. Morehead, J. Roos, L. M. Peter, C. Scheu and T. Bein, *Phys. Chem. Chem. Phys.*, 2014, **16**, 24610–24620.

43 (*a*) J. Kruger, R. Plass, M. Gratzel, P. J. Cameron and L. M. Peter, *J. Phys. Chem. B*, 2003, **107**, 7536–7539; (*b*) J. C. Byers, S. Ballantyne, K. Rodionov, A. Mann and O. A. Semenikhin, *ACS Appl. Mater. Interfaces*, 2011, **3**, 392–401.

44 (*a*) G. Garcia-Belmonte, A. Munar, E. M. Barea, J. Bisquert, I. Ugarte and R. Pacios, *Org. Electron.*, 2008, **9**, 847–851; (*b*) G. Garcia-Belmonte, P. P. Boix, J. Bisquert, M. Sessolo and H. J. Bolink, *Sol. Energy Mater. Sol. Cells*, 2010, **94**, 366–375.

45 (*a*) T. T. Thao, T. Q. Trung, V.-V. Truong and N. N. Dinh, Enhancement of Power Efficiency and Stability of P3HT-Based Organic Solar Cells under Elevated Operating-Temperatures by Using a Nanocomposite Photoactive Layer, *J. Nanomater.*, 2015, 463565; (*b*) D. R. G. Mitchell, G. Triani and Z. Zhang, Hydrothermal crystallization of amorphous titania films deposited using low temperature atomic layer deposition, *Thin Solid Films*, 2008, **516**, 8414–8423.

46 (*a*) C. G. Morales-Guio, S. D. Tilley, H. Vrubel, M. Gratzel and X. Hu, Hydrogen evolution from a copper(I) oxide photocathode coated with an amorphous molybdenum sulphide catalyst, *Nat. Commun.*, 2014, **5**, 3059; (*b*) B. Seger, T. Pedersen, A. B. Laursen, P. C. K. Vesborg, O. Hansen and I. Chorkendorff, Using TiO_2 as a Conductive Protective Layer for Photocathodic H_2 Evolution, *J. Am. Chem. Soc.*, 2013, **135**, 1057–1064.

47 (*a*) R. Meszaros, L. Thompson, M. Bos and P. de Groot, Adsorption and Electrokinetic Properties of Polyethylenimine on Silica Surfaces, *Langmuir*, 2002, **18**, 6164–6169; (*b*) E. Poptoshev and P. M. Claesson, Forces between Glass Surfaces in Aqueous Polyethylenimine Solutions, *Langmuir*, 2002, **18**, 2590–2594.

48 (*a*) P. C. Griffiths, A. Paul, P. Stilbs and E. Petterson, Charge on Poly(ethylene imine): Comparing Electrophoretic NMR Measurements and pH Titrations, *Macromolecules*, 2005, **38**, 3539–3542; (*b*) G. J. M. Koper and M. Borkovec, Proton binding by linear, branched, and hyperbranched polyelectrolytes, *Polymer*, 2010, **51**, 5649–5662.

49 (*a*) J. Jiaa, A. WuA and S. Luan, Spectrometry recognition of polyethyleneimine towards heavy metal ions, *Colloids Surf., A*, 2014, **449**, 1–7; (*b*) V. N. Kislenko and L. P. Oliynyk, Complex Formation of Polyethyleneimine with Copper(II), Nickel(II), and Cobalt(II) Ions, *J. Polym. Sci., Part A: Polym. Chem.*, 2002, **40**, 914–922.

50 H. Kang, S. Jung, S. Jeong, G. Kim and K. Lee, Polymer-metal hybrid transparent electrodes for flexible electronics, *Nat. Commun.*, 2015, **6**, 6503.

51 W. Septina, Gunawan, S. Ikeda, T. Harada, M. Higashi, R. Abe and M. Matsumura, Photosplitting of Water from Wide-Gap Cu(In,Ga)S_2 Thin Films Modified with a CdS Layer and Pt Nanoparticles for a High-Onset-Potential Photocathode, *J. Phys. Chem. C*, 2015, **119**, 8576–8583.

52 C. Li, T. Hisatomi, O. Watanabe, M. Nakabayashi, N. Shibata, K. Domen and J.-J. Delaunay, Positive onset potential and stability of Cu_2O-based photocathodes in water splitting by atomic layer deposition of a Ga_2O_3 buffer layer, *Energy Environ. Sci.*, 2015, **8**, 1493–1500.

53 M. J. Donachie Jr, *Titanium: A Technical Guide*, ASM International, Ohio, 2000, p. 125.

54 (*a*) S. Mazloomi and N. Sulaiman, Influencing factors of water electrolysis electrical efficiency, *Renewable Sustainable Energy Rev.*, 2012, **16**, 4257–4263; (*b*) Z. Lu, Y. Li, X. Lei, J. Liu and X. Sun, Ultrahigh Hydrogen Evolution Performance of Under-Water "Superaerophobic" MoS_2 Nanostructured Electrodes, *Adv. Mater.*, 2014, **26**, 2683–2687.

55 R. H. Coridan, A. C. Nielander, S. A. Francis, M. T. McDowell, V. Dix, S. M. Chatman and N. S. Lewis, Methods for Comparing the Performance of Energy-Conversion Systems for Use in Solar Fuels and Solar Electricity Generation, *Energy Environ. Sci.*, 2015, **8**, 2886–2901.